Approximation of acoustic black holes with finite element mixed formulations and artificial neural network correction terms

Arnau Fabra[§,†], Oriol Guasch[‡*], Joan Baiges[§], Ramon Codina[§,†]

[§] *Universitat Politècnica de Catalunya, Barcelona Tech, Jordi Girona 1-3, Edifici C1, 08034 Barcelona, Spain.*
[†] *Centre Internacional de Mètodes Numèrics en Enginyeria (CIMNE), Edifici C1, Campus Nord UPC, Gran Capità S/N, 08034 Barcelona, Spain.*
[‡] *Human-Environment Research (HER) group, La Salle, Universitat Ramon Llull, C/ Quatre Camins 30, 08022 Barcelona, Catalonia, Spain*

Abstract

Wave propagation in elastodynamic problems in solids often requires fine computational meshes. In this work we propose to combine stabilized finite element methods (FEM) with an artificial neural network (ANN) correction term to solve such problems on coarse meshes. Irreducible and mixed velocity-stress formulations for the linear elasticity problem in the frequency domain are first presented and discretized using a variational multiscale FEM. A non-linear ANN correction term is then designed to be added to the FEM algebraic matrix system and produce accurate solutions when solving elastodynamics on coarse meshes. As a case study we consider acoustic black holes (ABHs) on beams and plates. ABHs are traps for flexural waves based on reducing the structural thickness according to a power-law profile at the end of a beam, or within a two-dimensional circular indentation in a plate. For the ABH to function properly, the thickness at the termination/center must be very small, which demands very fine computational meshes. The proposed strategy combining the stabilized FEM with the ANN correction allows us to accurately simulate the response of ABHs on coarse meshes for values of the ABH order and residual thickness outside the training test, as well as for different excitation frequencies.

Keywords: Elastodynamics, Stabilized finite element methods, Vector-tensor mixed formulation, Artificial neural network, Acoustic black holes

1. Introduction

Under the infinitesimal strain assumption, linear elasticity can be studied using different sets of variables and formulations. It is most common to use the displacement as the unknown variable when working with the irreducible problem, or to work with displacement-stress or displacement-strain approaches for mixed formulations (see, e.g. [1–3]). Alternatively, velocity can also be considered instead of displacement for irreducible or mixed elasticity problems [4–7]. The latter are usually solved in the time domain, but by means of the time Fourier transform of the equations involved, the elasticity problem can be posed in the frequency domain. This is equivalent to assuming a harmonic time dependence of the problem variables. In the frequency domain, the number of variables is doubled, since their real and imaginary parts have to be considered [8, 9].

In this work, we will use the mixed velocity-stress formulation and its irreducible counterpart for the velocity [10], in combination with an artificial neural network (ANN) strategy [11], to be able to work on coarse meshes with problems that usually require very fine meshes. As an example of such problems we will

*Corresponding author.
Email addresses: afabra@cimne.upc.edu (Arnau Fabra[§,†]), oriol.guasch@salle.url.edu (Oriol Guasch[‡]), joan.baiges@upc.edu (Joan Baiges[§]), ramon.codina@upc.edu (Ramon Codina[§,†])

deal with wave propagation in acoustic black holes (ABHs) in beams and plates [12]. Let us discuss these three aspects of the current work in more detail.

The velocity-stress formulation for linear elasticity in [10] has some advantages over the displacement-stress one for wave phenomena, because it directly gives us a mixed vector-tensor analogue of the well-known scalar-vector mixed wave equation in acoustics [13–15]. In contrast, a displacement-stress approach results in a second-order form for the displacements and a zero-order one for stresses, from which a first-order mixed wave equation cannot be recovered. The weak form of the velocity-stress problem admits two main possibilities, namely the primal and dual formulations, depending on whether the term containing the divergence of the stresses or the divergence of the velocities is integrated by parts. In the first case, more regularity is obtained for the velocity than for the stresses, while the opposite is true for the dual problem.

The discretization of the variational elasticity problems in this work will be carried out using the finite element method (FEM). In general, the well-posedness of the problems at the continuum level is not inherited by their discretized counterparts. As far as the weak irreducible form of the problem is concerned, the Galerkin FEM usually provides stable and optimally convergent results, except for high frequencies, where the so-called pollution error may appear, as is the case with the Helmholtz equation [16–20]. However, this topic is outside the scope of this paper. On the other hand, for the discretization of the weak mixed form to be well posed, the finite elements must satisfy a discrete inf-sup condition that can be circumvented by resorting to stabilized formulations. The variational multiscale (VMS) stabilizing methods [21, 22] will be adopted in this paper. VMS are based on dividing the unknowns of the problem into two different scales, a large one that can be solved by the finite element mesh and a smaller subgrid scale (SGS) that cannot be captured by the mesh. The idea is to approximate the SGS components in terms of the finite element unknown components inside the elements and at their boundaries to improve stability [20, 23].

The second ingredient of this paper concerns the use of correction terms based on an ANN. As it will be explained later, the computation of wave motion in ABHs requires very fine meshes, so it would be interesting to make them coarser to reduce the computational cost. In [24] it was proposed to compare the solution of some benchmark problems on fine and coarse meshes and use them as training of an ANN to construct a correction term that could be applied to new simulations. With this term, valid solutions can be obtained with coarser meshes and therefore with a lower computational cost. To show the potential of the method, the case of static deflection of a beam with large deformations, the case of vortex shedding for an incompressible flow past a cylinder, and a simple fluid-structure interaction problem were considered. Subsequently, the ANN strategy for FEM computations was applied to the wave equation in mixed and irreducible forms, and in the time and frequency domains [11]. ANN correction terms will be designed here for the mixed and irreducible linear elasticity problems in the frequency domain.

The third part of this paper deals with the application of the stabilized FEM strategy for linear elasticity and the ANN correction terms to simulate bending wave propagation in ABHs. ABHs typically consist of wedge tips in beams or circular indentations in plates whose thickness decreases towards their termination (ABH beam) or center (ABH plate) following a power law profile (see e.g, [25–27]). When a bending wave enters an ABH, its velocity slows down, while its wavelength and amplitude increase. In the ideal case of zero thickness at the ABH termination/center, it can be shown that the wave would take infinite time to reach there. Therefore, no reflection would occur and the structure would act as a *black hole* for bending waves. In practice, small imperfections in the thinner part of the ABH can totally ruin the effect, but placing a small viscoelastic damping layer there can lead to a very significant suppression of wave reflections and consequently of vibrations in the uniform regions of the beam/plate [28].

Solving wave propagation in ABHs with the FEM can be quite demanding, since the thickness of the termination/center must be very small and the wavelength is shortened in that region. This requires very fine FEM meshes, as the standard request of at least six nodes per wavelength must be met. Consequently, other numerical approaches have been applied to ABHs, mostly based on the Rayleigh-Ritz method with different types of basis functions. Mexican hat wavelets [29] and Morlet wavelets [30] have been proposed for ABH beams, while 2D Daubechies wavelets [31] have been suggested for ABH plates. Very accurate results have also been obtained using Gaussian basis functions for ABH beams [32] and plates [33]. These approaches have proven to be very efficient for ABHs of simple geometries such as ring-shaped ABHs [34], double-leaf ABHs [35] or annular ABHs in cylinders [36], and even for periodic arrays of ABHs [37, 38] intended for

wave manipulation purposes like bandgap formation, focusing, negative refraction and bi-refraction, and collimation.

It is worth mentioning that commercial FEM software has already been applied to many ABH problems, but dealing with simplifying assumptions such as the Euler-Bernouilli theory for beams or the Kirchhoff-Love theory for plates (see e.g., [39–41]). However, if ABHs are to be embedded in complex structural components commonly found in industry (see e.g., [42]) there is a clear need to develop FEM methods that can deal with them at a reasonable computational cost. This article presents a first step towards this goal by studying conventional ABHs but treating the full linear elasticity equations and using an ANN correction to obtain accurate results with fairly coarse meshes.

The paper is organized as follows. In section 2, several formulations for the linear elasticity problem are described along with their variational counterparts and finite element approximations. In section 3, the ANN correction term for the irreducible velocity and mixed velocity-stress FEM approximations is explained and implemented. Next, in section 4, the stabilized FEM plus ANN strategy is applied to six numerical examples dealing with ABHs in beams and plates. Finally, the conclusions close the paper in section 5.

2. Mixed and Irreducible formulations of the linear elasticity problem

In this section we briefly present the irreducible and mixed approaches to the linear elasticity problem in strong and variational forms. We also present the stabilized FEM for solving the latter. We build on earlier work by some of the authors in [10] and refer the reader to it for more details.

2.1. Boundary value differential problems in the frequency domain

Let us consider a spatial domain $\Omega \subset \mathbb{R}^d$, where $d = 2, 3$, with boundary $\partial\Omega$. We split $\partial\Omega$ into two disjoint sets Γ_v and Γ_σ, where the boundary conditions corresponding to the velocity $\boldsymbol{v}$ and the normal component of the Cauchy stress tensor $\boldsymbol{\sigma}$ will be enforced, respectively.

The elastic fourth order constitutive tensor of the material will be denoted by $\boldsymbol{C}$. In this work, we will consider linear elastic and isotropic materials, so $\boldsymbol{C}$ and its inverse are written as

$$\boldsymbol{C} = \frac{E}{1+\nu}\boldsymbol{I}_4 + \frac{\nu E}{(1+\nu)(1-2\nu)}\boldsymbol{I}_2 \otimes \boldsymbol{I}_2, \qquad \text{and} \qquad \boldsymbol{C}^{-1} := \frac{1+\nu}{E}\boldsymbol{I}_4 - \frac{\nu}{E}\boldsymbol{I}_2 \otimes \boldsymbol{I}_2, \tag{1}$$

where $\boldsymbol{I}_4$ is the fourth-rank identity tensor, $\boldsymbol{I}_2$ is the second-rank identity tensor, E is the Young modulus and ν the Poisson ratio. The intrinsic damping of the material is taken into account by means of a complex Young's modulus, $E' = E(1 + \mathrm{i}\eta) \in \mathbb{C}$, where η is the loss factor.

2.1.1. Irreducible form

The irreducible form of the problem in the frequency domain consists in finding $\boldsymbol{v} : \Omega \to \mathbb{C}^d$ such that

$$-\rho\,\omega^2 \boldsymbol{v} - \nabla \cdot \boldsymbol{C} : \nabla^S \boldsymbol{v} = \boldsymbol{f}, \tag{2}$$

where ρ is the density, ω is the angular frequency, ∇^S is the symmetric gradient of a vector field and $\boldsymbol{f}$ is the force term. The boundary conditions on Γ_v and Γ_σ are given by

$$\boldsymbol{v} = \boldsymbol{0} \;\text{ on }\; \Gamma_v, \qquad \boldsymbol{n} \cdot \boldsymbol{C} : \nabla^S \boldsymbol{v} = \boldsymbol{0} \;\text{ on }\; \Gamma_\sigma, \tag{3}$$

where $\boldsymbol{n}$ corresponds to the unit normal pointing outward from the domain.

2.1.2. Mixed form

The mixed form of the problem in the frequency domain is to find $\boldsymbol{v} : \Omega \to \mathbb{C}^d$ and $\boldsymbol{\sigma} : \Omega \to \mathbb{C}^d \otimes \mathbb{C}^d$ such that

$$-\mathrm{i}\,\rho\,\omega\,\boldsymbol{v} - \nabla \cdot \boldsymbol{\sigma} = \boldsymbol{f}, \tag{4}$$

$$-\mathrm{i}\,\omega\,\boldsymbol{C}^{-1} : \boldsymbol{\sigma} - \nabla^S \boldsymbol{v} = \boldsymbol{0}, \tag{5}$$

with boundary conditions

$$\boldsymbol{v} = \boldsymbol{0} \;\text{ on }\; \Gamma_v, \qquad \boldsymbol{n} \cdot \boldsymbol{\sigma} = \boldsymbol{0} \;\text{ on }\; \Gamma_\sigma. \tag{6}$$

2.2. Variational formulations in the frequency domain

Before presenting the variational formulation of the irreducible and mixed elasticity problems, let us introduce some notation. $\mathfrak{O}$ will denote a subdomain of Ω, $L^2(\mathfrak{O})$ the space of square integrable functions in $\mathfrak{O}$ (scalars, vectors or tensors), $H^1(\mathfrak{O})$ the space of functions in $L^2(\mathfrak{O})$ with derivatives in $L^2(\mathfrak{O})$ and $H(\mathrm{div},\mathfrak{O})$ the space of vector or tensor functions with components and divergence in $L^2(\mathfrak{O})$. The inner product of two functions in $L^2(\mathfrak{O})$ will be represented by $(\cdot,\cdot)_{\mathfrak{O}}$, with the notation simplification $(\cdot,\cdot)_{\Omega} \equiv (\cdot,\cdot)$, whereas the integral of the product of any two ordinary or generalized functions will be designated as $\langle\cdot,\cdot\rangle_{\mathfrak{O}}$, again with $\langle\cdot,\cdot\rangle_{\Omega} \equiv \langle\cdot,\cdot\rangle$. Let V_v and V_σ be the appropriate spaces for the velocity and the stresses, respectively, formed by complex-valued functions. $\boldsymbol{w}$ will denote a test function in V_v and $\boldsymbol{\eta}$ a test function in V_σ.

2.2.1. Irreducible form

The variational form of the irreducible equation in Eq. (2) with boundary conditions in Eq. (3) is unique and obtained, as usual, multiplying Eq. (2) by a test function $\boldsymbol{w}$, integrating over the domain Ω, and then integrating by parts the second term of the equation considering the boundary terms in Eq. (3). Taking $V_v = \{\boldsymbol{w} \in H^1(\Omega)^d \mid \boldsymbol{w} = \boldsymbol{0} \text{ on } \Gamma_v\}$, the problem is that of finding a complex valued $\boldsymbol{v} \in V_v$ such that

$$-\rho\,\omega^2(\boldsymbol{v},\boldsymbol{w}) + (\boldsymbol{C} : \nabla^S \boldsymbol{v}, \nabla^S \boldsymbol{w}) = \langle \boldsymbol{f}, \boldsymbol{w}\rangle, \tag{7}$$

for all $\boldsymbol{w} \in V_v$, with the boundary conditions

$$\begin{aligned} \boldsymbol{v} &= \boldsymbol{0}, \quad && \text{strongly imposed on } \Gamma_v, \\ \boldsymbol{n}\cdot\boldsymbol{C} : \nabla^S \boldsymbol{v} &= \boldsymbol{0}, \quad && \text{weakly imposed on } \Gamma_\sigma. \end{aligned}$$

Note that the $L^2(\Omega)$ inner product is not symmetric, but Hermitian, being defined as

$$(a,b) = \int_\Omega a\bar{b}\,\mathrm{d}\Omega,$$

for any two functions a, b, where $\bar{b}$ represents the complex conjugate of b.

2.2.2. Mixed form: variational forms I and II

Let us start defining the bilinear form $B([\boldsymbol{v},\boldsymbol{\sigma}],[\boldsymbol{w},\boldsymbol{\eta}]) = -\langle\nabla\cdot\boldsymbol{\sigma},\boldsymbol{w}\rangle - \langle\nabla^S\boldsymbol{v},\boldsymbol{\eta}\rangle$ and the linear form $L([\boldsymbol{w},\boldsymbol{\eta}]) = \langle\boldsymbol{f},\boldsymbol{w}\rangle$. The weak form of the mixed problem in Eqs. (4)-(5) with boundary conditions in Eq. (6) is not unique and depends on which term of $B([\boldsymbol{v},\boldsymbol{\sigma}],[\boldsymbol{w},\boldsymbol{\eta}])$ is integrated by parts. This determines a different regularity for the velocity and stress unknowns.

The primal formulation will be called **variational form I** (VFI) and corresponds to integrating by parts the first term of $B([\boldsymbol{v},\boldsymbol{\sigma}],[\boldsymbol{w},\boldsymbol{\eta}])$. Note that the functional setting for the velocity in the VFI will be the same as for the irreducible variational form in Eq. (7). Defining the spaces $V_v = \{\boldsymbol{w} \in H^1(\Omega)^d \mid \boldsymbol{w} = \boldsymbol{0} \text{ on } \Gamma_v\}$ and $V_\sigma = L^2(\Omega)^{d\times d}$ and considering $\boldsymbol{v},\boldsymbol{w} \in V_v$ and $\boldsymbol{\sigma},\boldsymbol{\eta} \in V_\sigma$, we can rewrite $B([\boldsymbol{v},\boldsymbol{\sigma}],[\boldsymbol{w},\boldsymbol{\eta}])$ as

$$\begin{aligned} B([\boldsymbol{v},\boldsymbol{\sigma}],[\boldsymbol{w},\boldsymbol{\eta}]) &= (\boldsymbol{\sigma},\nabla^S\boldsymbol{w}) - (\nabla^S\boldsymbol{v},\boldsymbol{\eta}) - \langle\boldsymbol{n}\cdot\boldsymbol{\sigma},\boldsymbol{w}\rangle_{\Gamma_\sigma} \\ &=: B_I([\boldsymbol{v},\boldsymbol{\sigma}],[\boldsymbol{w},\boldsymbol{\eta}]) - \langle\boldsymbol{n}\cdot\boldsymbol{\sigma},\boldsymbol{w}\rangle_{\Gamma_\sigma}. \end{aligned}$$

The weak imposition of the boundary condition $\boldsymbol{n}\cdot\boldsymbol{\sigma} = \boldsymbol{0}$ on Γ_σ allows us to obtain the VFI for the linear elasticity equations in Eqs. (4)-(5), supplemented by Eq. (6). This consists in finding $\boldsymbol{v} \in V_v$ and $\boldsymbol{\sigma} \in V_\sigma$ such that

$$-\mathrm{i}\,\omega\,\rho\,(\boldsymbol{v},\boldsymbol{w}) - \mathrm{i}\,\omega(\boldsymbol{C}^{-1} : \boldsymbol{\sigma},\boldsymbol{\eta}) + B_I([\boldsymbol{v},\boldsymbol{\sigma}],[\boldsymbol{w},\boldsymbol{\eta}]) = L([\boldsymbol{w},\boldsymbol{\eta}]), \quad \forall\ \boldsymbol{w} \in V_v, \boldsymbol{\eta} \in V_\sigma, \tag{8}$$

and with $\boldsymbol{v} = \boldsymbol{0}$ prescribed strongly on Γ_v.

The dual formulation referred to as **variational form II** (VFII) corresponds to integrating by parts the second term of $B([\boldsymbol{v},\boldsymbol{\sigma}],[\boldsymbol{w},\boldsymbol{\eta}])$. Introducing the spaces $V_v = L^2(\Omega)^d$ and $V_\sigma = \{\boldsymbol{\eta} \in H(\mathrm{div},\Omega) \mid \boldsymbol{n}\cdot\boldsymbol{\eta} = \boldsymbol{0} \text{ on } \Gamma_\sigma\}$ we rewrite $B([\boldsymbol{v},\boldsymbol{\sigma}],[\boldsymbol{w},\boldsymbol{\eta}])$ as

$$\begin{aligned} B([\boldsymbol{v},\boldsymbol{\sigma}],[\boldsymbol{w},\boldsymbol{\eta}]) &= -(\nabla\cdot\boldsymbol{\sigma},\boldsymbol{w}) + (\boldsymbol{v},\nabla\cdot\boldsymbol{\eta}) - \langle\boldsymbol{v},\boldsymbol{n}\cdot\boldsymbol{\eta}\rangle_{\Gamma_v} \\ &=: B_{II}([p,\boldsymbol{u}],[q,\boldsymbol{v}]) - \langle\boldsymbol{v},\boldsymbol{n}\cdot\boldsymbol{\eta}\rangle_{\Gamma_v}. \end{aligned}$$

If we now impose $\boldsymbol{v} = \boldsymbol{0}$ weakly on Γ_v, the VFII of the linear elasticity equations in Eqs. (4)-(5) with conditions in Eq. (6) reads: find $\boldsymbol{v} \in V_v$ and $\boldsymbol{\sigma} \in V_\sigma$ such that

$$-\mathrm{i}\,\omega\,\rho\,(\boldsymbol{v},\boldsymbol{w}) - \mathrm{i}\,\omega(\boldsymbol{C}^{-1}:\boldsymbol{\sigma},\boldsymbol{\eta}) + B_{II}([\boldsymbol{v},\boldsymbol{\sigma}],[\boldsymbol{w},\boldsymbol{\eta}]) = L([\boldsymbol{w},\boldsymbol{\eta}]), \quad \forall\ \boldsymbol{w} \in V_v, \boldsymbol{\eta} \in V_\sigma. \tag{9}$$

with $\boldsymbol{n}\cdot\boldsymbol{\sigma} = \boldsymbol{0}$ imposed strongly on Γ_σ.

Note that VFI provides more regularity for the velocity than for the stresses, while the opposite is true for VFII.

2.3. Finite element approximation

We assume that Ω is a polyhedral domain and that $\mathcal{T}_h = \{K\}$ is a partition of Ω into finite elements K of characteristic size h. We consider the family of finite element partitions $\{\mathcal{T}_h\}_{h>0}$ to be quasi-uniform. The L^2 inner product inside an element K will be represented by $(\cdot,\cdot)_K$ and by $(\cdot,\cdot)_{\partial K}$ on its boundary ∂K. The conformal FEM spaces that approximate $\boldsymbol{v}$ and $\boldsymbol{\sigma}$ are denoted as $V_{v,h} \subset V_v$ and $V_{\sigma,h} \subset V_\sigma$, respectively.

For the variational irreducible problem in Eq. (7), the standard Galerkin FEM will suffice for the problem at hand. However, for the variational mixed formulations VFI in Eq. (8) and VFII in Eq. (9), we will employ a stabilized FEM based on the VMS method [21, 22, 43] to circumvent the discrete inf-sup condition and use equal interpolation for the velocities and the stresses. In the VMS, we introduce SGS spaces for $\boldsymbol{v}$ and $\boldsymbol{\sigma}$, namely, V_v' and V_σ', which complement the finite element ones so that $V_v = V_{v,h} \oplus V_v'$ and $V_\sigma = V_{\sigma,h} \oplus V_\sigma'$. The unknowns of the problem and their respective test functions are then split into a FEM part and a SGS part, such that $\boldsymbol{v} = \boldsymbol{v}_h + \boldsymbol{v}'$, $\boldsymbol{w} = \boldsymbol{w}_h + \boldsymbol{w}'$, $\boldsymbol{\sigma} = \boldsymbol{\sigma}_h + \boldsymbol{\sigma}'$ and $\boldsymbol{\eta} = \boldsymbol{\eta}_h + \boldsymbol{\eta}'$. Herafter, the prime will be used to denote SGS functions and SGS spaces. The key to the VMS is to find suitable approximations for the SGSs that stabilize and improve the Galerkin FEM solution.

2.3.1. Irreducible form

As already mentioned, for the variational irreducible problem we will work with frequencies low enough not to be affected by the pollution error. Therefore, the Galerkin FEM will produce the expected results with acceptable accuracy. The latter consists in finding $\boldsymbol{v}_h \in V_{v,h}$ such that

$$-\rho\,\omega^2(\boldsymbol{v}_h,\boldsymbol{w}_h) + (\boldsymbol{C}:\nabla^S\boldsymbol{v}_h,\nabla^S\boldsymbol{w}_h) = \langle\boldsymbol{f},\boldsymbol{w}_h\rangle, \qquad \forall \boldsymbol{w}_h \in V_{v,h}. \tag{10}$$

2.3.2. Mixed form

In this case, VMS stabilization must be used. Before that, let us introduce the differential operator $\mathcal{L} = [\mathcal{L}_v, \mathcal{L}_\sigma]$ and its transpose $\mathcal{L}^{\mathrm{t}} = [\mathcal{L}_v^{\mathrm{t}}, \mathcal{L}_\sigma^{\mathrm{t}}]$,

$$\begin{aligned}
\mathcal{L}_v([\boldsymbol{v}_h,\boldsymbol{\sigma}_h]) &= -\mathrm{i}\,\rho\,\omega\,\boldsymbol{v}_h - \nabla\cdot\boldsymbol{\sigma}_h, & \mathcal{L}_\sigma([\boldsymbol{v}_h,\boldsymbol{\sigma}_h]) &= -\mathrm{i}\,\omega\,\boldsymbol{C}^{-1}:\boldsymbol{\sigma}_h - \nabla^S\boldsymbol{v}_h,\\
\mathcal{L}_v^{\mathrm{t}}([\boldsymbol{w}_h,\boldsymbol{\eta}_h]) &= -\mathrm{i}\,\rho\,\omega\,\boldsymbol{w}_h + \nabla\cdot\boldsymbol{\eta}_h, & \mathcal{L}_\sigma^{\mathrm{t}}([\boldsymbol{w}_h,\boldsymbol{\eta}_h]) &= -\mathrm{i}\,\omega\,\boldsymbol{C}^{-1}:\boldsymbol{\eta}_h + \nabla^S\boldsymbol{w}_h.
\end{aligned}$$

These expressions allow us to write the differential equations of the mixed problem Eqs. (4)-(5) as $\mathcal{L}([\boldsymbol{v}_h,\boldsymbol{\sigma}_h]) = [\boldsymbol{f},\boldsymbol{0}]$. Note that the adjoint of $\mathcal{L}$ is the complex conjugate of $\mathcal{L}^{\mathrm{t}}$, although we will write the stabilized FEM formulation in terms of $\mathcal{L}^{\mathrm{t}}$.

The procedure for obtaining the VMS-FEM approximations to the variational forms VFI and VFII will not be given here and the reader is referred to [10] for details (see also [43], among others). However, we will present the final stabilized VMS-FEM forms to highlight the differences between VFI and VFII.

Splitting the unknowns $\boldsymbol{v}$ and $\boldsymbol{\sigma}$ into their FEM and SGS components and integrating by parts the terms containing derivatives of the SGSs, the stabilized FEM formulation for the VFI involves finding $\boldsymbol{v}_h \in V_{v,h}$ and $\boldsymbol{\sigma}_h \in V_{\sigma,h}$ such that

$$\begin{aligned}
&-\mathrm{i}\,\rho\,\omega\,(\boldsymbol{v}_h,\boldsymbol{w}_h) - \mathrm{i}\,\omega(\boldsymbol{C}^{-1}:\boldsymbol{\sigma}_h,\boldsymbol{\eta}_h) + B_I([\boldsymbol{v}_h,\boldsymbol{\sigma}_h],[\boldsymbol{w}_h,\boldsymbol{\eta}_h])\\
&\quad + \sum_K(\boldsymbol{v}',\mathcal{L}_v^{\mathrm{t}}([\boldsymbol{w}_h,\boldsymbol{\eta}_h]))_K + \sum_K(\boldsymbol{\sigma}',\mathcal{L}_\sigma^{\mathrm{t}}([\boldsymbol{w}_h,\boldsymbol{\eta}_h]))_K = L([\boldsymbol{w}_h,\boldsymbol{\eta}_h]),
\end{aligned} \tag{11}$$

for all $[\boldsymbol{w}_h, \boldsymbol{\eta}_h] \in V_{v,h} \times V_{\sigma,h}$.

Likewise, the stabilized FEM formulation for VFII entails finding $\boldsymbol{v}_h \in V_{v,h}$ and $\boldsymbol{\sigma}_h \in V_{\sigma,h}$ such that

$$
\begin{aligned}
&-\mathrm{i}\,\rho\,\omega\,(\boldsymbol{v}_h, \boldsymbol{w}_h) - \mathrm{i}\,\omega(\boldsymbol{C}^{-1} : \boldsymbol{\sigma}_h, \boldsymbol{\eta}_h) + B_{II}([\boldsymbol{v}_h, \boldsymbol{\sigma}_h], [\boldsymbol{w}_h, \boldsymbol{\eta}_h]) \\
&\quad + \sum_K (\boldsymbol{v}', \mathcal{L}_v^{\mathrm{t}}([\boldsymbol{w}_h, \boldsymbol{\eta}_h]))_K + \sum_K (\boldsymbol{\sigma}', \mathcal{L}_\sigma^{\mathrm{t}}([\boldsymbol{w}_h, \boldsymbol{\eta}_h]))_K = L([\boldsymbol{w}_h, \boldsymbol{\eta}_h]),
\end{aligned} \tag{12}
$$

for all $[\boldsymbol{w}_h, \boldsymbol{\eta}_h] \in V_{v,h} \times V_{\sigma,h}$.

The velocity and stress SGSs $\boldsymbol{v}'$ and $\boldsymbol{\sigma}'$ in the interiors of the elements in Eqs. (11)-(12) are approximated respectively by,

$$
\boldsymbol{v}'|_K = \tau_v \tilde{P}_h[\boldsymbol{f} - \mathcal{L}_v([\boldsymbol{v}_h, \boldsymbol{\sigma}_h])]_K, \tag{13}
$$

$$
\boldsymbol{\sigma}'|_K = \tau_\sigma \tilde{P}_h[-\mathcal{L}_\sigma([\boldsymbol{v}_h, \boldsymbol{\sigma}_h])]_K, \tag{14}
$$

where τ_v and τ_σ are stabilization parameters (see [10] for their expressions) and two different options can be considered for the projection $\tilde{P}_h$. If the space of SGSs is chosen as the space of finite element residuals, then $\tilde{P}_h = I$, with I being the identity, and the stabilization approach is known as the algebraic subgrid scale (ASGS) method (see e.g., [44]). On the other hand, if the space of SGSs is considered to be orthogonal to the finite element space, the projection in Eqs. (13)-(14) becomes $\tilde{P}_h = I - P_h$, with P_h standing for the projection onto the finite element space. The resulting method is known as the orthogonal subgrid scale (OSGS) method (see e.g., [45]).

3. A correction technique using artificial neural networks

As mentioned in the introduction, many problems, such as the bending motion of ABH beams and plates that we are concerned with in this paper, require fine computational meshes. Therefore, if a parametric analysis involving a large number of simulations is to be performed, the computational cost can become prohibitive. In this section, we adapt the ANN strategy in [11, 24] to the current linear elasticity problem in irreducible and mixed forms. The key idea is to compute a set of solutions to variations of the original problem on fine meshes (e.g., by making changes to the geometry and physical parameters), and then use them to derive a correction term that improves the result of simulations on coarse meshes, which include variations not previously considered. The first phase is the training of the ANN and the second is the testing (or execution).

Let us first present the algebraic matrix systems for the discrete irreducible and mixed forms of the problem, and then explain how to compute the ANN correction term.

3.1. Algebraic structure of the irreducible and mixed elasticity problems

Suppose that we have either discretized the FEM problem in Eq. (10) or in Eqs. (11) and (12) using a coarse mesh. In all cases, the resulting linear algebraic matrix system will be of the type,

$$
\mathsf{A}\mathsf{U}_{\mathrm{c}} = \mathsf{F}, \tag{15}
$$

where $\mathsf{U}_{\mathrm{c}} \in \mathbb{C}^m$ is the unknown vector of nodal values and $\mathsf{F} \in \mathbb{C}^m$ is the force one. m is the product of the total number of nodes by the number of degrees of freedom of each node, i.e., the total number of degrees of freedom of the problem. The matrix of the system has dimensions $m \times m$ and it is complex, i.e., $\mathsf{A} \in \mathbb{C}^{m \times m}$. Given F and A, the unknown vector U_{c} can be computed from Eq. (15) provided A is invertible. As mentioned above, our goal is to improve the accuracy of U_{c} by adding an ANN correction term to Eq. (15).

3.1.1. Matrix system for the irreducible form

The matrices and vectors of Eq. (15) for the FEM discretization of the irreducible formulation in Eq. (10) are

$$\mathsf{A} = -\omega^2 \mathsf{M}_v - \mathsf{K}_v, \quad \mathsf{F} = \mathsf{F}_v, \quad \mathsf{U}_\mathrm{c} = \mathsf{v},$$

where M_v is the mass matrix that includes the density and K_v is the stiffness matrix, which contains the material properties, see Eq. (1). F_v is the force vector and v is the unknown vector containing all the degrees of freedom of the mesh nodes corresponding to $\boldsymbol{v}_h$.

3.1.2. Matrix system for the mixed forms VFI and VFII

To facilitate the identification of the entries in the algebraic matrix systems for VFI and VFII in Eqs. (11) and (12), let us explicitly write the stabilization terms of these equations instead of making use of the differential operators $\mathcal{L}_v, \mathcal{L}_\sigma$. The stabilization terms read,

$$\begin{aligned}
&\sum_K \tau_v(\tilde{P}_h[\boldsymbol{f} + \mathrm{i}\,\omega\,\rho\,\boldsymbol{v}_h + \nabla\cdot\boldsymbol{\sigma}_h], \mathrm{i}\,\omega\,\rho\,\boldsymbol{w}_h + \nabla\cdot\boldsymbol{\eta}_h)_K \\
&+ \sum_K \tau_\sigma(\tilde{P}_h[\mathrm{i}\,\omega\,\boldsymbol{C}^{-1} : \boldsymbol{\sigma}_h + \nabla^S \boldsymbol{v}_h], \mathrm{i}\,\omega\,\boldsymbol{C}^{-1} : \boldsymbol{\eta}_h + \nabla^S \boldsymbol{w}_h)_K.
\end{aligned}$$

On the other hand, let us introduce some notation before setting A, U_c and F in Eq. (15) for VFI and VFII. Again, v refers to the vector of unknown degrees of freedom for the velocity, while s denotes that for the stress $\boldsymbol{\sigma}_h$. A is built from block matrices and a double subscript is used to indicate their position. That is, vv is a block matrix in the momentum equation that multiplies v, while $v\sigma$ represents a block matrix in the momentum equation multiplying s. Analogously, σv is a block matrix in the constitutive equation that multiplies v and $\sigma\sigma$ is a block matrix in the constitutive equation that multiplies s. As for the stabilization block matrices they are identified by a subscript τ and either a superscript label 'asgs' designating a term that only appears in the ASGS method, or an equivalent superscript 'osgs' for the OSGS. Moreover, G_S is the matrix that arises from the symmetric gradient and D that from the divergence of a tensor tested with a vector function.

The matrices and vectors in Eq. (15) for the mixed formulation VFI in Eq. (11) are given by,

$$\begin{aligned}
\mathsf{A} &= \begin{bmatrix} -\mathrm{i}\,\omega\,\mathsf{M}_{vv} + \omega^2 \mathsf{M}^{\mathrm{asgs}}_{\tau,vv} + \mathsf{S}_{\tau,vv} & -\mathrm{i}\,\omega\,\mathsf{M}^{\mathrm{asgs}}_{\tau,v\sigma} + \mathrm{i}\,\omega\,\mathsf{S}^{\mathrm{asgs}}_{\tau,v\sigma} + \mathsf{G}^{\mathrm{t}}_S \\ -\mathrm{i}\,\omega\,\mathsf{M}^{\mathrm{asgs}}_{\tau,\sigma v} + \mathrm{i}\,\omega\,\mathsf{S}^{\mathrm{asgs}}_{\tau,\sigma v} - \mathsf{G}_S & -\mathrm{i}\,\omega\,\mathsf{M}_{\sigma\sigma} + \omega^2 \mathsf{M}^{\mathrm{asgs}}_{\tau,\sigma\sigma} + \mathsf{S}_{\tau,\sigma\sigma} \end{bmatrix}, \\
\mathsf{F} &= \begin{bmatrix} \mathsf{f} + \mathsf{f}^{\mathrm{osgs}}_{\tau,v}(\mathsf{v}) \\ \mathrm{i}\,\omega\,\mathsf{f}^{\mathrm{asgs}}_{\tau} + \mathsf{f}^{\mathrm{osgs}}_{\tau,\sigma}(\mathsf{s}) \end{bmatrix}, \qquad \mathsf{U}_\mathrm{c} = \begin{bmatrix} \mathsf{v} \\ \mathsf{s} \end{bmatrix},
\end{aligned} \tag{16}$$

while A for VFII in Eq. (12) becomes

$$\mathsf{A} = \begin{bmatrix} -\mathrm{i}\,\omega\,\mathsf{M}_{vv} + \omega^2 \mathsf{M}^{\mathrm{asgs}}_{\tau,vv} + \mathsf{S}_{\tau,vv} & -\mathrm{i}\,\omega\,\mathsf{M}^{\mathrm{asgs}}_{\tau,v\sigma} + \mathrm{i}\,\omega\,\mathsf{S}^{\mathrm{asgs}}_{\tau,v\sigma} - \mathsf{D} \\ -\mathrm{i}\,\omega\,\mathsf{M}^{\mathrm{asgs}}_{\tau,\sigma v} + \mathrm{i}\,\omega\,\mathsf{S}^{\mathrm{asgs}}_{\tau,\sigma v} + \mathsf{D}^{\mathrm{t}} & -\mathrm{i}\,\omega\,\mathsf{M}_{\sigma\sigma} + \omega^2 \mathsf{M}^{\mathrm{asgs}}_{\tau,\sigma\sigma} + \mathsf{S}_{\tau,\sigma\sigma} \end{bmatrix},$$

with F and U_c being the same as for VFI.

3.2. Artificial neural network correction

Let us next solve our linear elasticity problem using a finer mesh than that of Eq. (15), which provides the solution $\mathsf{U}_\mathrm{f} \in \mathbb{C}^M$ with $M \gg m$. We can construct a projection from the space to which the fine solution belongs to the space of the coarse solution,

$$\mathsf{P}_\mathrm{fc} : \mathbb{C}^M \longrightarrow \mathbb{C}^m.$$

This projection is essential for our ANN correction term since we assume that the best possible solution in the coarse mesh is given by $\mathsf{U}_\mathrm{c} = \mathsf{P}_\mathrm{fc}(\mathsf{U}_\mathrm{f})$.

For a linear problem, it is easy to introduce a correction $\mathsf{D}_\mathrm{ex} \in \mathbb{C}^m$ to Eq. (15) to obtain the solution $\mathsf{P}_\mathrm{fc}(\mathsf{U}_\mathrm{f})$. We simply have to consider

$$\mathsf{A}\mathsf{U}_\mathrm{c} + \mathsf{D}_\mathrm{ex} = \mathsf{F} \quad \text{with} \quad \mathsf{D}_\mathrm{ex} = \mathsf{F} - \mathsf{A}\mathsf{P}_\mathrm{fc}(\mathsf{U}_\mathrm{f}), \tag{17}$$

which has solution $\mathsf{U}_\mathrm{c} = \mathsf{P}_\mathrm{fc}(\mathsf{U}_\mathrm{f})$, provided A is invertible.

Obviously, if we need to solve a single problem, the procedure of Eq. (17) does not make sense since we already have U_f. However, as explained at the beginning of the section our interest is to solve variations of the original problem on coarse grids to save computational costs. The idea is to first solve some of them on fine meshes (ANN training) and then construct the correction terms to resolve new variations of the problem on coarse meshes (ANN testing).

Let us next focus on the ANN training. Suppose that we have N variations of the original problem for which we have computed the fine solutions, $\mathsf{U}_{\mathrm{f},\alpha}$, $\alpha = 1, \ldots, N$, with each value of α denoting a particular variation. The *uncorrected* coarse problem for each one is

$$\mathsf{A}_\alpha \mathsf{U}_{\mathrm{c},\alpha} = \mathsf{F}_\alpha, \quad \alpha = 1, \ldots, N.$$

Introducing the *exact* correction

$$\mathsf{D}_{\mathrm{ex},\alpha} = \mathsf{F}_\alpha - \mathsf{A}_\alpha \mathsf{P}_\mathrm{fc}(\mathsf{U}_{\mathrm{f},\alpha}), \quad \alpha = 1, \ldots, N, \tag{18}$$

we obtain the *corrected* solution to the coarse problems

$$\mathsf{A}_\alpha \mathsf{U}_{\mathrm{c},\alpha} + \mathsf{D}_{\mathrm{ex},\alpha} = \mathsf{F}_\alpha, \tag{19}$$

given by $\mathsf{U}_{\mathrm{c},\alpha} = \mathsf{P}_\mathrm{fc}(\mathsf{U}_{\mathrm{f},\alpha})$, $\forall\ \alpha = 1, \ldots, N$.

The set of solutions $\mathsf{U}_{\mathrm{c},\alpha} = \mathsf{P}_\mathrm{fc}(\mathsf{U}_{\mathrm{f},\alpha})$ constitutes the *training set* and the associated variations, $\{\alpha\}$, are called the *training configurations*. The goal now is to design a correction term $\mathsf{D} \in \mathbb{C}^m$ that can improve the coarse solution for any variation not contemplated in the training configurations. That is, we are looking for a correction D such that the solution of

$$\mathsf{A}\mathsf{U}_\mathrm{c} + \mathsf{D} = \mathsf{F},$$

improves that of Eq. (15). Our proposal for the correction term is that it only depends on the unknown solution, i.e., $\mathsf{D} = \mathsf{D}(\mathsf{U}_\mathrm{c})$, and that it has to be as "close" as possible to $\mathsf{D}_{\mathrm{ex},\alpha}$ from the training configurations. Therefore, the problem to be solved has the form

$$\mathsf{A}\mathsf{U}_\mathrm{c} + \mathsf{D}(\mathsf{U}_\mathrm{c}) = \mathsf{F}. \tag{20}$$

Different options could be considered for $\mathsf{D}(\mathsf{U}_\mathrm{c})$ (see e.g., [11]), and ours has been to use an ANN. The latter offers several advantages regarding, for example, the flexibility and stability to complete the training set to improve the correction term, with little computational effort (among others). The ANN aims to fit the inputs $\{\mathsf{P}_\mathrm{fc}(\mathsf{U}_{\mathrm{f},\alpha})\}_{\alpha=1}^N$ and the outputs $\{\mathsf{D}_{\mathrm{ex},\alpha}\}_{\alpha=1}^N$ given by Eq. (18). The ANN construction of $\mathsf{D}(\mathsf{U}_\mathrm{c})$ consists of a highly nonlinear mapping

$$\mathsf{D} : \mathbb{C}^m \longrightarrow \mathbb{C}^m,$$

trained with the pairs $\{\mathsf{P}_\mathrm{fc}(\mathsf{U}_{\mathrm{f},\alpha}), \mathsf{D}_{\mathrm{ex},\alpha}\}_{\alpha=1}^N$. For the elasticity problem at hand, it has been sufficient to use simple network architectures, with only a few hidden layers and a few neurons per layer. We have considered feedforward architectures with backpropagation algorithms to compute weights and biases, with the sigmoid function being the choice for the activation function.

To apply ANNs to our problem we have to define three important factors: the input to the network, its output and the loss function. The input is the set $\{\mathsf{P}_\mathrm{fc}(\mathsf{U}_{\mathrm{f},\alpha})\}_{\alpha=1}^N$ but, since $\mathsf{P}_\mathrm{fc}(\mathsf{U}_{\mathrm{f},\alpha})$ is the vector of nodal

values of a certain function $u_{c,\alpha}(\boldsymbol{x})$ defined on the coarse mesh, we can introduce some simplifications in our FEM framework. For example, when trying to obtain the j-th component of D, namely D_j, $j = 1, \ldots, m$, it makes sense to use only some components of $\mathsf{P}_{\mathrm{fc}}(\mathsf{U}_{\mathrm{f},\alpha})$. In the present work we select those associated to the nodes connected to the one involving the jth degree of freedom. The influence of these neighboring nodes can be taken into account by including the derivatives of $u_{c,\alpha}(\boldsymbol{x})$ as an input to the ANN. Note that the output of the network are precisely the D_j entries of D. As for the loss function of the ANN, which determines its weights and biases, it is constructed as

$$\mathcal{C} = \sum_{\alpha=1}^{N} \|\mathsf{D}_{\mathrm{ex},\alpha} - \mathsf{D}(\mathsf{P}_{\mathrm{fc}}(\mathsf{U}_{\mathrm{f},\alpha}))\|^2. \tag{21}$$

This makes explicit that the ANN is trained with the configurations for which the exact correction is known.

Once the correction term D has been built, we need to solve Eq. (20), which is strongly non-linear because of its dependence on U_{c}, for new variations in A and/or F (ANN testing). This can be done through the iterative strategy,

$$\mathsf{A}{\mathsf{U}_{\mathrm{c}}}^{(k)} = \mathsf{F} - \mathsf{D}({\mathsf{U}_{\mathrm{c}}}^{(k-1)}), \tag{22}$$

where the superscript k is the iteration counter. This simple approach has worked for our problem, but alternatives, such as the Newton-Raphson scheme, could have been used instead.

4. Application: Acoustic black holes in beams and plates

4.1. General considerations

In the following we will apply the stabilized FEM formulation for the linear elasticity problem and the ANN correction term to calculate the bending motion in ABH beams and plates. The thickness profile of the classical ABH wedge of a beam, or that of a circular ABH indentation, is a power law,

$$h(r) = \frac{h_{\mathrm{uni}} - h_0}{r_{\mathrm{abh}}^m} |r|^m + h_0, \tag{23}$$

where h_0 is the residual thickness at the end of the ABH beam (or at the center of the indentation for ABH plates), h_{uni} is the thickness of the uniform part of the beam (plate), r_{abh} is the length (radius) of the ABH and m its order. Note that $h(r_{\mathrm{abh}}) = h_{\mathrm{uni}}$ and that $h(0) = h_0$ (see Fig. 1 for a schematic of an ABH beam).

We will train the ANN on fine meshes to obtain a good FEM solution when we vary a parameter of the ABH and simulate on coarser meshes. In particular, we will consider changing the ABH oder, m, its residual thickness, h_0, and the frequency of the incident wave. In all the examples we will work with the mixed formulation VFI, although an ANN training with the irreducible form will be also carried out for the ABH beam, for comparison purposes.

As far as the ANN is concerned, and as explained in section 3.2, a simple architecture with a few hidden layers and few neurons per layer has been sufficient for our purposes. To avoid under and over-fitting, the parameters of the ANN have been carefully chosen for each case, keeping in mind that generating very complex models is not the goal of this work. The number of layers and neurons will be specified below for each example. It is worth mentioning that one of the main difficulties we encountered with this type of training has been the sharp increase in the values of the variables when approaching an eigenvalue. Although the damping layer smooths them significantly, these large changes in solution values make ANN training challenging. However, as will be demonstrated in the results of the next subsections, good results have been obtained despite this problem.

The improvement of the coarse mesh solution with the ANN correction term has been evaluated by characterizing it with the percentage index,

$$I = \frac{E_c - E_t}{E_c} \times 100, \tag{24}$$

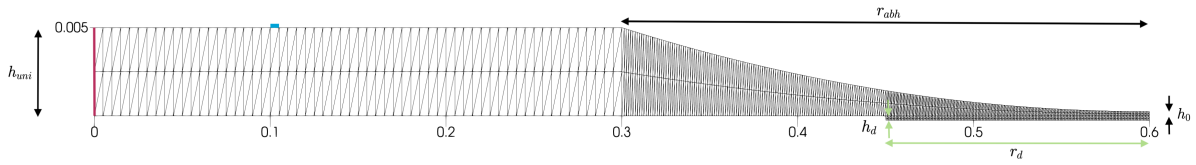

Figure 1: 2D geometry of the ABH beam and coarse FEM mesh.

where E_c refers to the error of the solution computed on the coarse mesh compared to the solution on the fine mesh, and E_t refers to the error of the solution computed on the coarse mesh but using the correction term from the trained ANN. The errors have been computed for invariants under coordinate transformations. That is, the modulus has been used for the real and imaginary parts of the velocity independently, while the Frobenius norm and the trace have been calculated for the real and imaginary parts of the stress tensor.

4.2. Acoustic black hole at a beam termination

Typically, the Euler-Bernouilli theory is used when simulating bending wave motion in ABH beams (see e.g., [32, 46, 47], among many others), which results in a one dimensional (1D) problem. In this paper we deal with the full linear elasticity equations and the ABH beam could be simulated in 3D. However, to reduce the computational cost and to get a faster sensing when training the ANN, the ABH beam will be simulated as a 2D system. In the following section, a full 3D model for the ABH plate will be used.

The geometry of the 2D ABH beam along with its coarsest mesh (2160 linear elements) is shown in Fig. 1. The beam has a length of 0.6 m and its thickness in the uniform portion is $h_{\text{uni}} = 0.005$ m. The size of the ABH wedge is $r_{\text{abh}} = 0.3$ m and its residual thickness will be specified for each example below, as well as its order m. The beam has a density $\rho_b = 1000$ kg/m^3, a Young modulus of $E_b = 10 \times 10^9$ N/m^2, loss factor $\eta_b = 0.3$ and Poisson's coefficient $\nu_b = 0.28$. As for the damping layer to dissipate vibrational energy, it is placed at the end of the ABH and has a length $r_d = 0.15$ m and thickness $h_d = 0.00025$ m. Its physical parameters are $\rho_d = 1000$ kg/m^3, $E_d = 10 \times 10^9$ N/m^2, $\eta_d = 0.3$ and $\nu_d = 0.28$.

Regarding the boundary conditions, the left end of the ABH beam (red line in Fig. 1) is considered to be clamped, so all components of the velocity are set to zero. The right end is left free. A load is applied to the beam at $x = 0.1$ m (blue line in Fig. 1), which is imposed as a Dirichlet condition with value $\boldsymbol{v} = (0, -1)$ m/s. The frequency of the excitation, f (resp. ω) will be indicated in each example. The cut-on frequency of the ABH in this case is $f_{\text{cut-on}} = 136.2$ Hz ($\omega_{\text{cut-on}} = 855.5$ rad/s) so the ABH is expected to be effective for $f \gtrsim 3f_{\text{cut-on}}$ ($\omega \gtrsim 3\omega_{\text{cut-on}}$) see e.g., [33].

In what concerns the ANN correction, we have chosen the gradients of the velocity components as inputs to the ANN in all the 2D examples in this section for simplicity, leaving aside the stresses. However, we will see that as a result of the ANN correction, not only does the velocity field improve substantially, but also the stress tensor. Regarding the output of the ANN, the correcting term has been applied to all the equations.

4.2.1. ABH beam: training for the order m

As a first example we consider computing the vibration of an ABH beam with a given order m (see Eq. (23)), on a coarse mesh and for an angular frequency of excitation $\omega = 4200$ rad/s and a residual thickness $h_0 = 0.00025$. For this, we need to train the ANN to construct the correction term computing the solution of the problem on fine meshes and using a training set for the m-parameter, which consists of m values ranging from $m = 2.4$ to $m = 3$ with steps $\Delta m = 0.02$. The fine mesh for the training phase has 34560 elements, while the coarse mesh for testing is 16 times smaller and has 2160 elements (see Fig. 1). A simple ANN with 3 layers and 3 neurons per layer has been used to build the correction term, with a learning momentum of 0.2. The number of maximum epochs has been set to 5000 and the maximum tolerated error is 1. The testing is performed for an ABH order of $m = 2.61$, which does not belong to the training set, and using the coarse mesh.

	m training improvement mixed	m training improvement irreducible	h_0 training improvement mixed	ω training improvement mixed
$\|\Re\{\boldsymbol{v}\}\|$	48.21%	70.83%	57.38%	45.36%
$\|\Im\{\boldsymbol{v}\}\|$	61.91%	96.54%	71.33%	57.56%
$\|\Re\{\boldsymbol{\sigma}\}\|_{\mathrm{F}}$	80.61%	-	38.93%	82.43%
$\|\Im\{\boldsymbol{\sigma}\}\|_{\mathrm{F}}$	75.27%	-	51.58%	86.45%
$\mathrm{tr}\{\Re\{\boldsymbol{\sigma}\}\}$	78.88%	-	54.00%	79.12%
$\mathrm{tr}\{\Im\{\boldsymbol{\sigma}\}\}$	74.74%	-	50.70%	85.17%

Table 1: Percentage improvement index I of Eq. (24) for the 2D ABH beam cases using the modulus of the real and imaginary parts of the velocity vector and the Frobenius norm and trace of the real and imaginary parts of the stress tensors.

For completeness, the same example has been run for the irreducible formulation instead of VFI. The former is less accurate than the latter and requires finer meshes to obtain similar results. Specifically, the fine mesh in this case has 138240 elements, while 8640 elements are used in the coarse mesh. As for the ANN, it has 3 layers with 4 neurons per layer, a learning momentum of 0.4, a maximum number of epochs of 2000 and a tolerance error of 1.

The percentage improvement index I in Eq. (24) for each problem variable when using the ANN correction for both the irreducible and mixed VFI forms is shown in Table 1. As observed in the first two columns of the table, the results of the problem improve significantly without exceptions. The values of I are satisfactory for the mixed formulation and remarkable for the irreducible one.

In Fig. 2, we show plots for the real and imaginary parts of the y-component of the velocity along the length of the beam for the trained, coarse and fine cases and using both the VFI formulation (Figs. 2a and b, top row) and the irreducible one (Figs. 2c and d, bottom row). It can be seen from the two top row plots for VFI that the effect of the ANN correction is noticeable; the trained solution provides a much closer solution to the fine one than the coarse solution with no ANN term. The trained solution matches the fine one in amplitude and also in phase, capturing the rise in amplitude and the decrease in wavelength as the wave approaches the ABH termination. Regarding the irreducible formulation of the bottom row, it is observed that the coarse solution provides a really bad approximation to the fine solution for both the real and imaginary parts of the vertical component of the velocity. The trained solution clearly improves the real part of the coarse one (see Fig. 2c) and is almost identical to the fine solution for the imaginary part (see Fig. 2d).

Concerning the computational times of this example, and to make them independent of the available computational resources, let us consider that a simulation with a single set of parameter values on the fine mesh for VFI corresponds to 100% of the computational time. The same computation on the coarse mesh costs 1.17%. On the other hand, the training phase with the ANN correction costs only 105.24%, while for the execution phase we have 1.27%. In the case of the irreducible form, and again taking as reference the simulation on the fine mesh (100% of the cost), we have a running time of 4.56% for the coarse mesh, 110.14% for the ANN training and 5.20% for the execution phase. This means that by investing more or less the time of a computation on the fine mesh (those in the training phase are only slightly longer) one can then perform a large number of computations on a coarse mesh in the execution phase with high accuracy and very reasonable computational costs (basically those of solving directly on a coarse mesh). The percentages of the computational times of the following examples are very similar to these, so the above explanation also applies to them.

4.2.2. ABH beam: training for the residual thickness h_0

In this second case, the unknown parameter is the residual thickness h_0. Therefore, we need to train our model using ABHs with various values of h_0 for fixed ABH order (we take the quadratic case $m = 2$) and an excitation angular frequency $\omega = 4200$ rad/s. The training set for h_0 ranges from $h_0 = 0.00025$ m to $h_0 = 0.001$ m at $\Delta h_0 = 0.000025$ m intervals. The fine mesh for training is smaller than in the previous

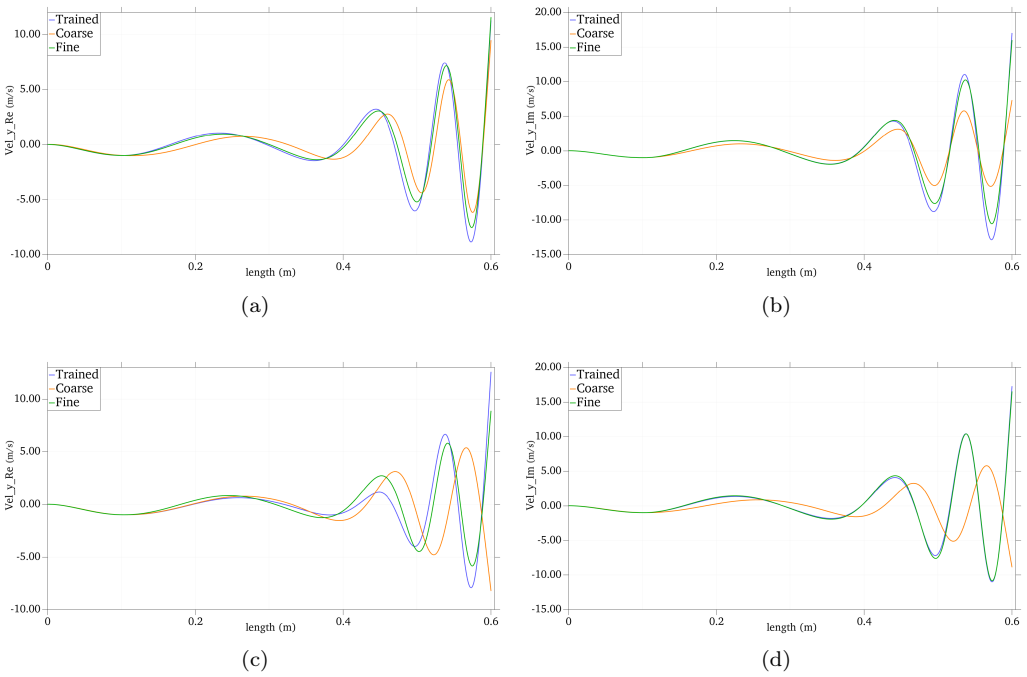

Figure 2: Real (left) and imaginary (right) parts for the y-component of the velocity along the ABH length (x axis) at $y = 0$. Results of the ABH order m training computed with the mixed VFI formulation (top row, (a)-(b)) and the irreducible one (bottom row (c)-(d)).

case and has 8640 elements, while the coarse mesh is the same (2160 elements). As for the ANN, it contains 3 layers with 4 neurons each, has a learning momentum of 0.2 and we have considered a maximum number of epochs of 5000 with a tolerance error of 1.

The execution phase to test the performance of the ANN correction has been run with $h_0 = 0.00046$ m, which again does not belong to the training set. Hereafter we have only worked with the VFI formulation. The improvement index I for this example is shown in the third column of Table 1. Again, I is remarkable for the two norms and the traces.

In Fig. 3, we plot again the real and imaginary parts of the y-component of the velocity along the length of the ABH beam for the trained, coarse and fine cases. The trained solution markedly improves the coarse solution, which is out of phase with the fine solution and produces much larger amplitudes. For the imaginary part in Fig. 3b, it can be seen how the coarse solution presents an additional peak which is 180° out of phase with the correct solution at the ABH tip, while the trained solution follows the trend of fine one.

4.2.3. ABH beam: training for the excitation frequency

In this third example we set the order of the ABH to $m = 2$ and its residual thickness to $h_0 = 0.00025$ m. The training set is the range of angular frequencies $[3700, 4200]$ rad/s at intervals of $\Delta\omega = 4$ rad/s. We have used the same fine and coarse meshes as in the previous example. The ANN has 3 layers with 4 neurons each, a learning momentum of 0.1, a maximum number of epochs of 10000 and an error tolerance of 1. For the execution phase we have used the frequency $\omega = 4002$ rad/s, which is not in the training set.

The index I for this example is shown in the fourth column of Table 1. Again, the index for the two norms and for the traces exhibit a remarkable improvement without exception. In addition, and as for the two previous examples, in Fig. 4 we have plotted the real and imaginary parts of the vertical component of the velocity along the ABH beam for the trained, coarse and fine cases. Of all the examples, this is the one where the coarse case without the ANN correction gives a better solution, which is quite close to the fine

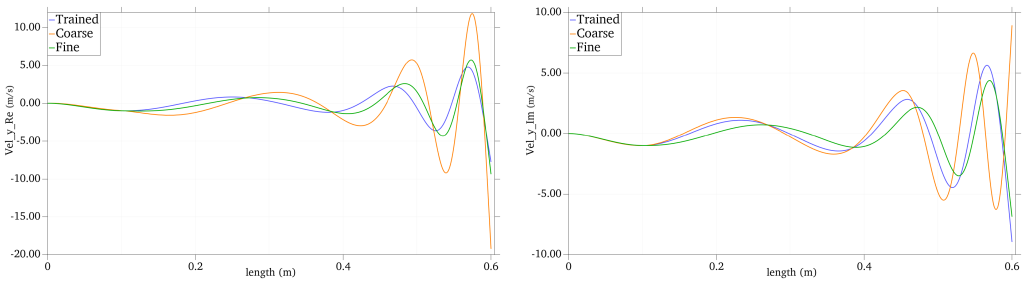

(a) (b)

Figure 3: Real (a) and imaginary (b) parts for the y-component of the velocity along the ABH length (x axis) at $y = 0$. Results of the residual thickness h_0 training computed with the mixed VFI formulation.

solution for the real part of the velocity (see Fig. 4a). This is not so obvious for the imaginary part of the velocity (see Fig. 4b). However, in any case the coarse solution can compete with the trained one, whose results are much closer to the fine solution in terms of amplitude and wavelength.

4.3. Acoustic black hole indentation on a plate

As with ABH beams, most works in literature use simplified theories to deal with ABHs embedded in plates. The Kirchhoff-Love thin plate theory is widely employed (see e.g., [31, 33, 48]) since it allows dealing with a 2D rather than a 3D problem. However, and as mentioned before, full 3D simulations will be carried out in this section to characterize ABH plates.

The geometry of the ABH plate for the simulations in this section, as well as its coarser mesh are shown in Fig. 5. The ABH plate has dimensions $L_x \times L_y = 0.9 \times 1$ m^2 with a thickness $h_{\text{uni}} = 0.005$ m in the uniform part. The ABH indentation has radius $r_{\text{abh}} = 0.3$ m and it is placed at the center of the plate, where it has residual thickness h_0 (to be specified in each example). The damping layer is squared with size $L_d = 0.15$ m and thickness $h_d = 0.00025$ m. The physical parameters of the ABH plate are as follows. It has density $\rho_p = 1190$ kg/m^3, Young modulus $E_p = 3.2 \times 10^9$ N/m^2, loss factor $\eta_p = 0.005$ and Poisson's coefficient $\nu_p = 0.3$. For the damping layer we take $\rho_d = 950$ kg/m^3, $E_d = 5 \times 10^9$ N/m^2, $\eta_d = 0.3$ and $\nu_d = 0.3$.

As for the boundary conditions, all sides of the plate are clamped (the velocity is imposed to be zero in all the directions). An excitation load is applied on the small pink area of Fig. 5(a) as a Dirichlet condition with value $\boldsymbol{v} = (0, 0, -1)$ m/s. Its frequency will be determined for each case study. The cut-on frequency

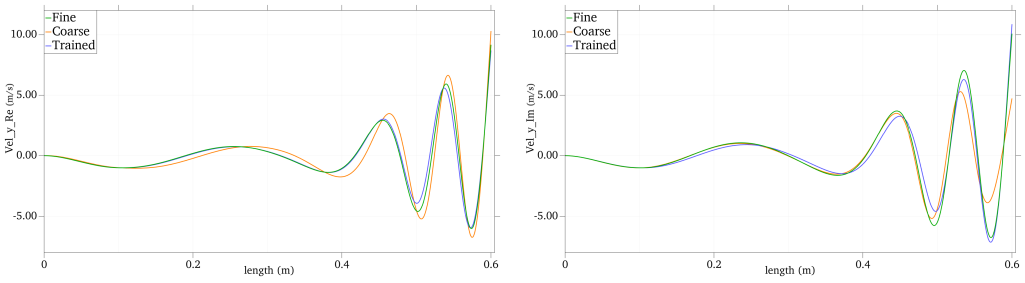

(a) (b)

Figure 4: Real (a) and imaginary (b) parts for the y-component of the velocity along the ABH length (x axis) at $y = 0$. Results of the frequency ω training computed with the mixed VFI formulation.

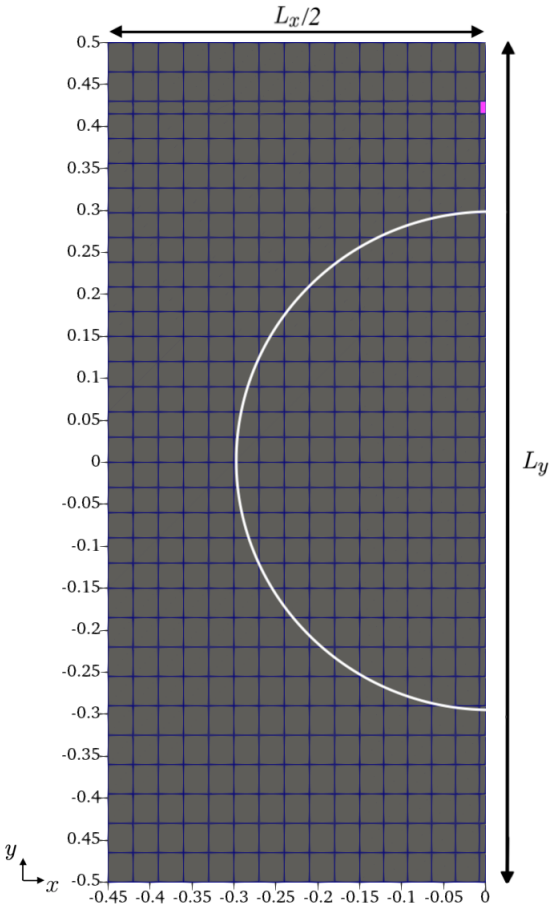

(a) Geometry of the xy plane.

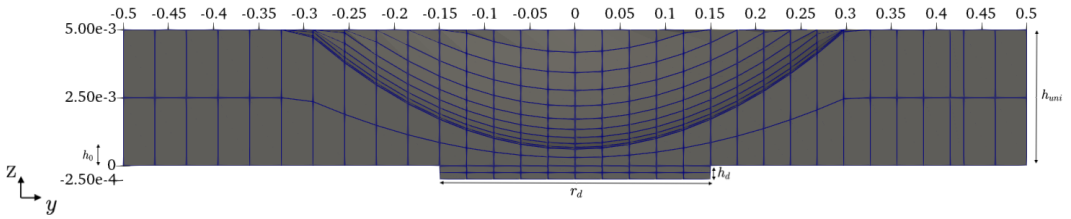

(b) Scaled geometry of the yz plane.

Figure 5: 3D geometry of the ABH plate and coarse FEM mesh.

of the ABH plate is $f_{\text{cut-on}} = 143.3$ Hz ($\omega_{\text{cut-on}} = 272$ rad/s), so again the ABH is expected to be effective for $f \gtrsim 3f_{\text{cut-on}}$ ($\omega \gtrsim 3\omega_{\text{cut-on}}$).

Concerning the ANN correction term, we have chosen the velocity components as ANN inputs in all 3D examples, again discarding the stresses. However, only ANN outputs that include stresses will be taken. Yet, the z components of the latter will be excluded due to the poor resolution of the mesh in the z direction. As will be demonstrated, this particular configuration for the ANN correction term will improve all problem variables (velocities and stresses) in the execution phase, when solving the problem on coarse meshes.

Finally, it should be mentioned that it has not been possible to use the irreducible formulation to calculate the ABH plate vibration due to the occurrence of transverse shear locking effects (see e.g., [49–51], as well as the survey [52]). Therefore, only the mixed VFI formulation will be considered in the following examples.

	m training improvement mixed	h_0 training improvement mixed	ω training improvement mixed
$\|\Re\{\boldsymbol{v}\}\|$	46.50%	56.79%	73.64%
$\|\Im\{\boldsymbol{v}\}\|$	36.57%	61.87%	70.58%
$\|\Re\{\boldsymbol{\sigma}\}\|_{\mathrm{F}}$	59.36%	14.04%	14.23%
$\|\Im\{\boldsymbol{\sigma}\}\|_{\mathrm{F}}$	15.17%	8.84%	20.12%
$\mathrm{tr}\{\Re\{\boldsymbol{\sigma}\}\}$	70.60%	31.79%	31.07%
$\mathrm{tr}\{\Im\{\boldsymbol{\sigma}\}\}$	60.03%	16.07%	50.58%

Table 2: Percentage improvement index I of Eq. (24) for the 3D ABH beam cases using the modulus of the real and imaginary parts of the velocity vector and the Frobenius norm and trace of the real and imaginary parts of the stress tensors.

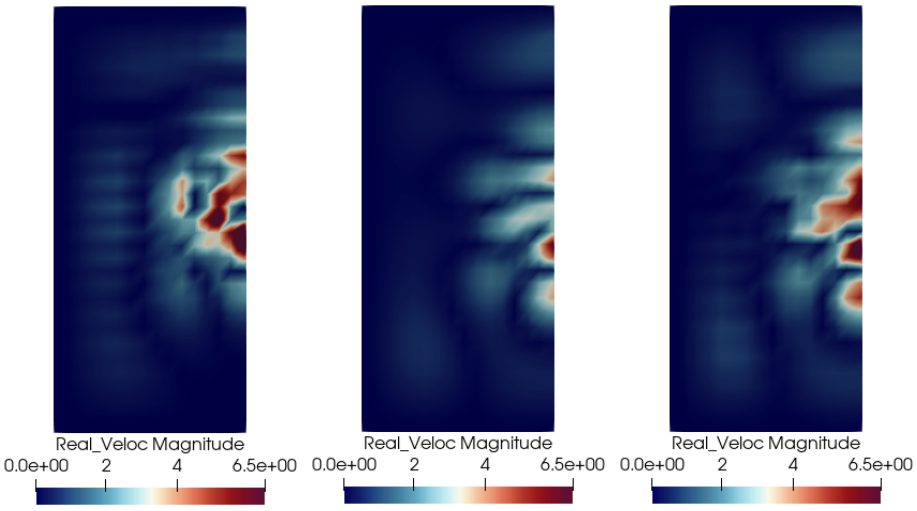

(a) Coarse. (b) Fine. (c) Trained.

Figure 6: Magnitude of the real part the velocity vector in the top xy surface of the ABH plate. Results of the order m training for the ABH plate.

We have observed that this locking effect disappears using the mixed velocity-stress formulation employed in this paper, similarly to what happens using the mixed displacement-stress formulation studied in [53].

4.3.1. ABH plate: training for the order m

In this example, we proceed analogously to the first example for the ABH beam by training the ANN with different values of the ABH order, m, which varies from $m = 2$ to $m = 3$ at intervals of $\Delta m = 0.02$. For the training phase we used a mesh with 9152 elements, which is eight times finer than the coarse one for the execution phase that only has 1144 elements (see Fig. 5). An ANN model of 3 layers with 3 neurons each has been implemented, with a learning momentum of 0.7, a maximum number of epochs of 10000 and a tolerance error of 1. The angular frequency of excitation has been set to $\omega = 900$ rad/s and the residual thickness to $h_0 = 0.00025$ m.

The testing phase has been carried out for a value of $m = 2.81$, not belonging to the training set. The improvement index I of this example is shown in the first column of Table 2. All values are more than acceptable except for the Frobenius norm of the imaginary part of the stress tensor, which has a relatively lower value.

To better appreciate the effects of the ANN correction, in Figs. 6 a,b and c, the results for the z-component of the real part of the ABH plate velocity are plotted for the coarse, fine and trained cases. The

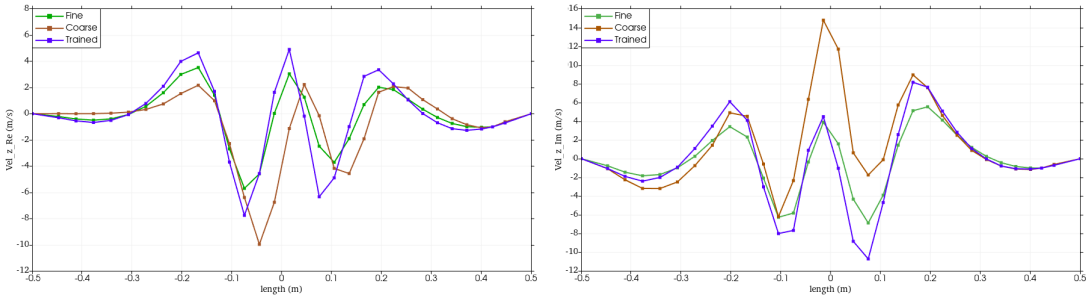

(a) (b)

Figure 7: Real (a) and imaginary (b) parts of the z-component of the velocity for the coarse, fine and trained cases over a line joining the the points $(0, -0.5, 0)$ and $(0, 0.5, 0)$. Results of the order m training for the ABH plate.

trained solution is qualitatively closer to the fine one than the coarse solution without correction term. For completion, in Fig. 7, we have plotted the real and imaginary parts of the z-component of the velocity along the straight line joining the points $(0, -0.5, 0)$ and $(0, 0.5, 0)$ for the trained, coarse and fine cases. This line is of special interest because it passes through the point where the external load is applied and through the center of the ABH, so it is a good indicator of how the vibrations are concentrated inside the ABH. As can be seen in the figure and for the real part of the velocity, the trained solution is able to correct the significant phase error of the coarse one when compared to the fine solution. As for the imaginary part of the velocity, the trained solution greatly improves the amplitude error exhibited by the coarse solution.

With regard to the computational times of this example, we get very similar percentage results to those of the ABH beam examples. Taking as reference the computation on the fine mesh (100% of the computational time), we obtain 1.36% for the coarse mesh, 102.12% for the training phase and 1.42% for the execution phase. Therefore, with essentially the cost of a fine computation (the training phase is not much longer) at the beginning, we can ultimately perform several tests on a coarse mesh with high accuracy and very low computational cost (execution phase). The computational times of the following examples are very similar to these ones and will be not specified, this explanation also being valid for them.

4.3.2. ABH plate: training for the residual thickness h_0

As was done previously for the beam, we now focus on the residual thickness h_0. To this purpose we have proceeded analogously to the previous example for the ABH plate, using the same fine and coarse meshes. The ANN architecture is also the same, with a slight change in the learning momentum from 0.7 to 0.6. The excitation angular frequency has been set to $\omega = 850$ rad/s and the ABH order to $m = 2$. The training set for h_0 goes from $h_0 = 0.00025$ m to $h_0 = 0.001$ m at intervals of $\Delta h_0 = 0.000025$ m.

In the execution phase we have worked with the value of $h_0 = 0.00061$ m, which was not previously considered in the training set. Index I in this example is shown in the second column of Table 2. As observed, the improvement is noticeable for the norms of the real and imaginary parts of the velocity, but much weaker for the Frobenius norm and trace of the stress tensor.

In Figs. 8 a,b and c, the results for the norm of the real part of the velocity in the coarse, fine and trained cases are plotted in the xy plane, respectively. It can be qualitatively observed how the trained solution is closer to the fine one than the coarse solution, correcting for the amplitude of the oscillations at the center of the ABH. In Fig. 9, we plot the real and imaginary parts of the z-component of the velocity along the same line than in the previous example. In this figure it can be better observed how the trained solution clearly improves the amplitude of the oscillations within the ABH provided by the coarse solution.

4.3.3. ABH plate: training for the excitation frequency

As a final example for the ABH plate we consider changing the excitation frequency as we did for the ABH beam. Once again, we use the same fine and coarse 3D meshes as in the previous cases. As for the

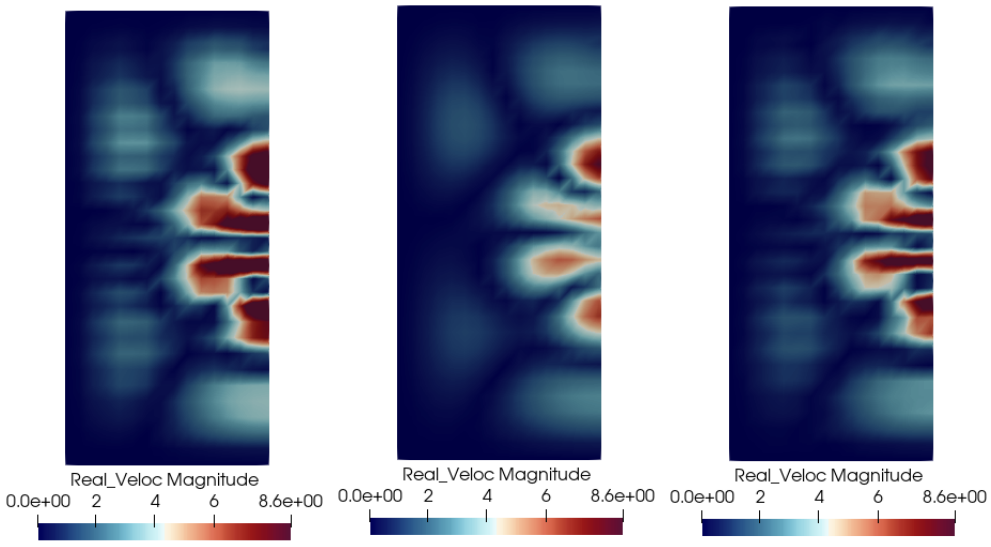

(a) Coarse. (b) Fine. (c) Trained.

Figure 8: Magnitude of the real part the velocity vector in the top xy surface of the domain for the numerical example. Results of the residual thickness h_0 training for the ABH plate.

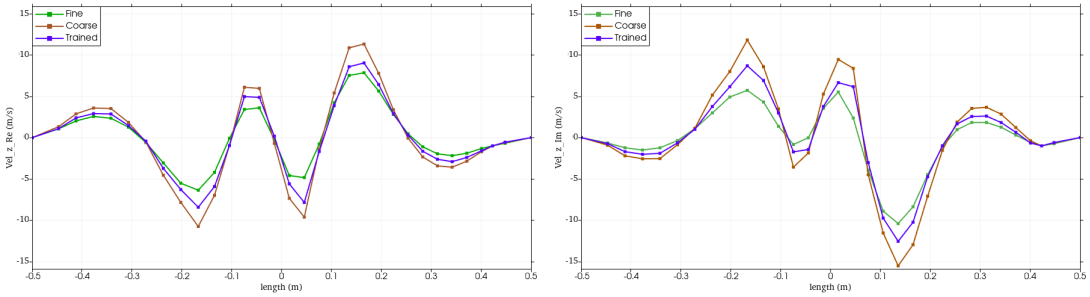

(a) (b)

Figure 9: Real (a) and imaginary (b) parts of the z-component of the velocity for the coarse, fine and trained cases over a line joining the the points $(0, -0.5, 0)$ and $(0, 0.5, 0)$. Results of the residual thickness h_0 training for the ABH plate.

ANN architecture, we have employed that of the first ABH plate example but with a maximum number of epochs of 1000. The residual thickness of the ABH plate has been set to $h_0 = 0.00025$ m and the ABH order to $m = 2$. The training phase sweeps the excitation frequency from $\omega = 700$ rad/s to $\omega = 1200$ rad/s at intervals of 10 rad/s.

The execution phase was launched with a frequency of $\omega = 835$ rad/s, which does not appear in the training set. The improvement index I for this case is found in the third column of Table 2. Its values are similar to those found when training for the residual thickness h_0, with remrkable improvement in the real and imaginary parts of the velocity norms and the stress tensor traces. The indices based on the Frobenius norm are not as high as the others, but they are also positive.

In Figs. 10 a,b and c, we plot again the norm of the real part of the velocity in the coarse, fine and trained cases, respectively. As can be seen, the trained solution is much closer to the fine one than to the coarse one, strongly correcting the excessive amplitude of the latter. This is very clearly observed in Fig. 11, which represents the real and imaginary parts of the z-velocity component on the same straight line as the previous examples. The effectiveness of the ANN correction term is very apparent from the results in the

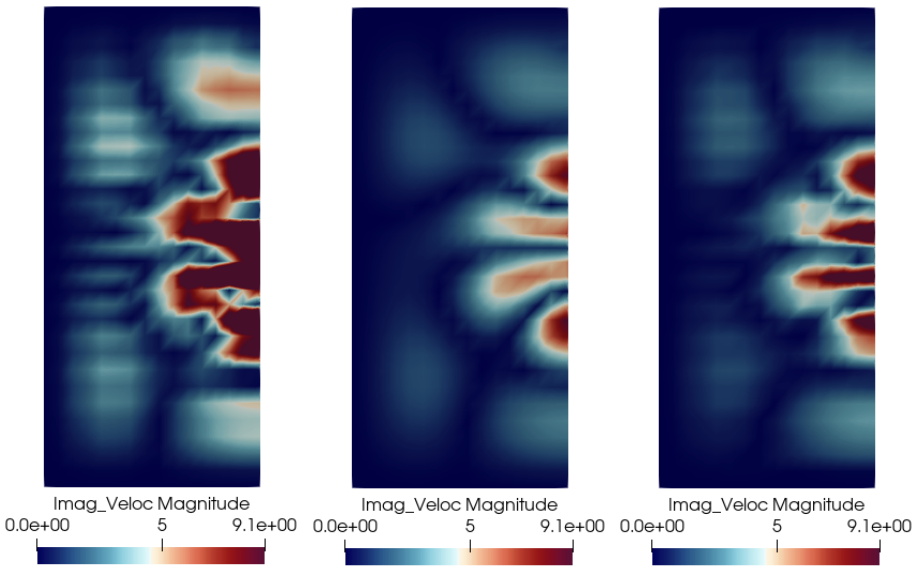

(a) Coarse. (b) Fine. (c) Trained.

Figure 10: Magnitude of the real part the velocity vector in the top xy surface of the domain for the numerical example. Results of the excitation frequency training for the ABH plate.

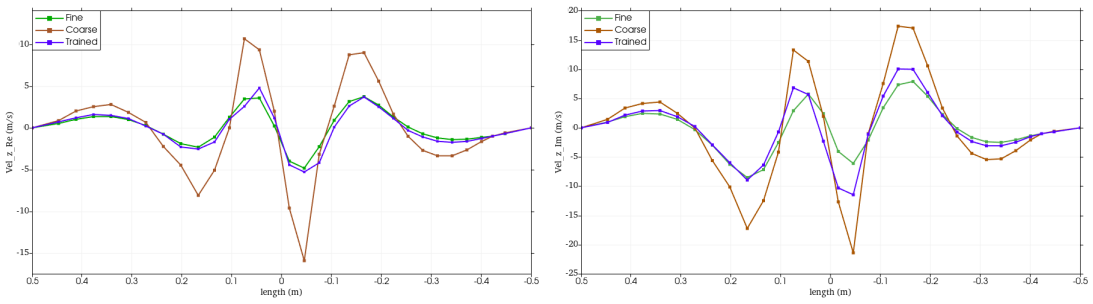

(a) (b)

Figure 11: Real (a) and imaginary (b) parts of the z-component of the velocity for the coarse, fine and trained cases over a line joining the the points $(0, -0.5, 0)$ and $(0, 0.5, 0)$. Results of the frequency ω training for the ABH plate.

figure.

5. Conclusions

In this paper we have proposed ANN correction terms to enhance the FEM solution of elastodynamics when solved on coarse meshes. We have started by presenting irreducible and mixed velocity-stress strong formulations for linear elastodynamic problems and their variational counterparts. The latter have been discretized using the FEM and a stabilized VMS-based formulation has been proposed for their primal and dual versions in order to use equal interpolation for the velocity and stress fields. An ANN correction term has been designed that results in a nonlinear algebraic matrix system for the discrete unknowns of the problem, so that that once a training phase with fine meshes and several sets of parameter values has been completed, it is able to properly solve an elastodynamic problem on a coarse mesh.

As examples of application, we have considered the vibrations of ABH beams and plates. Since ABHs have a very small residual thickness and the wavelength of impinging waves decreases as they approach it, very fine meshes are needed to compute their vibration under external harmonic loading. A first example consisting of an ABH termination in a 2D beam has been addressed. The ANN has been trained on fine meshes for three sets of parameters involving variations of the order of the ABH, its residual thickness and the frequency of the external loading. When solving the vibration of the ABH beam on a coarse mesh in the execution phase, for a previously untested parameter, significant magnitude and phase errors are encountered unless the ANN correction term is applied. The ANN solutions show a close resemblance to those calculated on fine meshes for both the irreducible and mixed primal (VFI) formulations (the dual one has not been used in the examples for the sake of brevity). As a second example, we have considered wave propagation in a 3D plate with an embedded circular ABH. Tests have been performed by again varying the order of the ABH, the residual thickness and the excitation frequency. Again, the ANN correction has shown significant enhancement of the solution in the execution phase, when computing the ABH plate response under external excitation for untested parameters on coarse meshes. However, the improvements for the ABH plate are, in general, not as good as for the ABH beam. It is to be mentioned that the irreducible variational form of the problem could not be applied to the ABH plate due to transverse shear locking. Therefore, only the results with the VFI have been presented for this example. The improvement index, which has been defined to determine the effect of the ANN correction for both the ABH beam and ABH plate, is in fact higher for the velocity field than for the stress field. This is logical since the VFI presents more regularity for the former than for the latter.

To date, ABHs have been designed mainly for beams, thin flat plates and cylindrical shells showing great potential for vibration and noise reduction. If they are to be embedded in more complex structures, it will be necessary to find finite element methods that can represent their behavior with relatively coarse meshes to lighten the computational cost. This work should be considered a first step towards that goal.

Acknowledgements

R. Codina gratefully acknowledges the support received through the ICREA Acadèmia Research Program of the Catalan Government. This work was partially funded through the TOP-FSI: RTI2018-098276-B-I00 project of the Spanish Government. CIMNE is a recipient of a "Severo Ochoa Programme for Centers of Excellence in R&D" grant (CEX2018-000797-S) by the Spanish Ministry of Economy and Competitiveness. O. Guasch acknowledges the support of the Generalitat de Catalunya (Departament de Recerca i Universitats) through grant 2021 SGR 1396 awarded to the HER group.

Declaration of generative AI and AI-assisted technologies in the writing process

During the preparation of this work the authors used DeepL in order to improve the English grammar of the manuscript. After using DeepL, the authors reviewed and edited the content as needed and take full responsibility for the content of the publication.

References

[1] R. Codina, Finite element approximation of the three field formulation of the Stokes problem using arbitrary interpolations, SIAM J. Numer. Anal.47 (2009) 699–718.

[2] M. Cervera, M. Chiumenti, R. Codina, Mixed stabilized finite element methods in nonlinear solid mechanics: Part I: Formulation, Comput. Methods Appl. Mech. Engrg.199 (37-40) (2010) 2559–2570.

[3] M. Chiumenti, M. Cervera, R. Codina, A mixed three-field finite element formulation for stress accurate analysis including the incompressible limit, Comput. Methods Appl. Mech. Engrg.283 (2015) 1095–1116.

[4] E. Bécache, P. Joly, C. Tsogka, An analysis of new mixed finite elements for the approximation of wave propagation problems., SIAM J. Numer. Anal.37, no. 4 (2000) 1053–1084.

[5] E. Bécache, P. Joly, C. Tsogka, A new family of mixed finite elements for the linear elastodynamic problem., SIAM J. Numer. Anal.39, no. 6 (2002) 2109–2132.

[6] G. Scovazzi, T. Song, X. Zeng, A velocity/stress mixed stabilized nodal finite element for elastodynamics: Analysis and computations with strongly and weakly enforced boundary conditions, Comput. Methods Appl. Mech. Engrg.325 (2017) 532–576.
[7] G. Festa, J.-P. Vilotte, The Newmark scheme as velocity–stress time-staggering: an efficient PML implementation for spectral element simulations of elastodynamics, Geophys. J. Int.161 (3) (2005) 789–812.
[8] P. D. Wilcox, A. Velichko, Efficient frequency-domain finite element modeling of two-dimensional elastodynamic scattering, J. Acoust. Soc. Am.127 (1) (2010) 155–165.
[9] J. T. de Freitas, Hybrid finite element formulations for elastodynamic analysis in the frequency domain, Int. J. Solids Struct.36 (13) (1999) 1883–1923.
[10] A. Fabra, R. Codina, Mixed stabilized finite element methods in linear elasticity for the velocity–stress equations in the time and the frequency domains, Comput. Methods Appl. Mech. Engrg.404 (2023) 115777.
[11] A. Fabra, J. Baiges, R. Codina, Finite element approximation of wave problems with correcting terms based on training artificial neural networks with fine solutions, Comput. Methods Appl. Mech. Engrg.399 (2022) 115280.
[12] A. Pelat, F. Gautier, S. C. Conlon, F. Semperlotti, The acoustic black hole: A review of theory and applications, J. Sound Vib.476 (2020) 115316.
[13] R. Codina, Finite element approximation of the hyperbolic wave equation in mixed form, Comput. Methods Appl. Mech. Engrg.197 (13-16) (2008) 1305–1322.
[14] S. Badia, R. Codina, H. Espinoza, Stability, convergence, and accuracy of stabilized finite element methods for the wave equation in mixed form, SIAM J. Numer. Anal.52 (4) (2014) 1729–1752.
[15] P. Monk, J. Schöberl, A. Sinwel, Hybridizing Raviart-Thomas elements for the Helmholtz equation, Electromagnetics 30 (1-2) (2010) 149–176.
[16] F. Ihlenburg, Finite element analysis of acoustic scattering, Springer, 1998.
[17] A. Deraemaeker, I. Babuška, P. Bouillard, Dispersion and pollution of the fem solution for the Helmholtz equation in one, two and three dimensions, Int. J. Numer. Meth. Engrg.46 (4) (1999) 471–499.
[18] I. Harari, F. Magoulès, Numerical investigations of stabilized finite element computations for acoustics, Wave Motion 39 (4) (2004) 339–349.
[19] O. Guasch, R. Codina, An algebraic subgrid scale finite element method for the convected Helmholtz equation in two dimensions with applications in aeroacoustics, Comput. Methods Appl. Mech. Engrg.196 (45-48) (2007) 4672–4689.
[20] J. Baiges, R. Codina, A variational multiscale method with subscales on the element boundaries for the Helmholtz equation, Int. J. Numer. Meth. Engrg.93 (6) (2013) 664–684.
[21] T. J. Hughes, Multiscale phenomena: Green's functions, the Dirichlet-to-Neumann formulation, subgrid scale models, bubbles and the origins of stabilized methods, Comput. Methods Appl. Mech. Engrg.127 (1-4) (1995) 387–401.
[22] T. J. Hughes, G. R. Feijóo, L. Mazzei, J.-B. Quincy, The variational multiscale method—A paradigm for computational mechanics, Comput. Methods Appl. Mech. Engrg.166 (1-2) (1998) 3–24.
[23] R. Codina, J. Principe, J. Baiges, Subscales on the element boundaries in the variational two-scale finite element method, Comput. Methods Appl. Mech. Engrg.198 (5-8) (2009) 838–852.
[24] J. Baiges, R. Codina, I. Castanar, E. Castillo, A finite element reduced-order model based on adaptive mesh refinement and artificial neural networks, Int. J. Numer. Meth. Engrg.121 (4) (2020) 588–601.
[25] M. Mironov, Propagation of a flexural wave in a plate whose thickness decreases smoothly to zero in a finite interval, Sov. Phys. Acoust.34 (3) (1988) 318–319.
[26] V. Krylov, F. Tilman, Acoustic 'black holes' for flexural waves as effective vibration dampers, J. Sound Vib.274 (3-5) (2004) 605–619.
[27] O'Boy, DJ and Krylov, Victor V, Damping of flexural vibrations in circular plates with tapered central holes, J. Sound Vib.330 (10) (2011) 2220–2236.
[28] V. V. Krylov, New type of vibration dampers utilising the effect of acoustic'black holes', Acta Acust. united Ac.90 (5) (2004) 830–837.
[29] L. Tang, L. Cheng, H. Ji, J. Qiu, Characterization of acoustic black hole effect using a one-dimensional fully-coupled and wavelet-decomposed semi-analytical model, J. Sound Vib.374 (2016) 172–184.
[30] P. Zeng, L. Zheng, J. Deng, A. Elsabbagh, S. Xiang, T. Yan, Y. Wu, Flexural wave concentration in tapered cylindrical beams and wedge-like rectangular beams with power-law thickness, J. Sound Vib.452 (2019) 82–96.
[31] L. Ma, S. Zhang, L. Cheng, A 2D Daubechies wavelet model on the vibration of rectangular plates containing strip indentations with a parabolic thickness profile, J. Sound Vib.429 (2018) 130–146.
[32] J. Deng, L. Zheng, P. Zeng, Y. Zuo, O. Guasch, Passive constrained viscoelastic layers to improve the efficiency of truncated acoustic black holes in beams, Mech. Syst. Signal Pr.118 (2019) 461–476.
[33] J. Deng, L. Zheng, O. Guasch, H. Wu, P. Zeng, Y. Zuo, Gaussian expansion for the vibration analysis of plates with multiple acoustic black holes indentations, Mech. Syst. Signal Pr.131 (2019) 317–334.
[34] J. Deng, O. Guasch, L. Zheng, Ring-shaped acoustic black holes for broadband vibration isolation in plates, J. Sound Vib.458 (2019) 109–122.
[35] L. Tang, L. Cheng, Ultrawide band gaps in beams with double-leaf acoustic black hole indentations, J. Acoust. Soc. Am.142 (5) (2017) 2802–2807.
[36] J. Deng, O. Guasch, L. Maxit, L. Zheng, Vibration of cylindrical shells with embedded annular acoustic black holes using the Rayleigh-Ritz method with Gaussian basis functions, Mech. Syst. Signal Pr.150 (2021) 107225.
[37] L. Tang, L. Cheng, Broadband locally resonant band gaps in periodic beam structures with embedded acoustic black holes, J. Appl. Phys.121 (19) (2017) 194901.
[38] J. Deng, O. Guasch, L. Zheng, Reconstructed Gaussian basis to characterize flexural wave collimation in plates with

periodic arrays of annular acoustic black holes, Int. J. Mech. Sci.194 (2021) 106179.
[39] S. C. Conlon, J. B. Fahnline, F. Semperlotti, Numerical analysis of the vibroacoustic properties of plates with embedded grids of acoustic black holes, J. Acoust. Soc. Am.137 (1) (2015) 447–457.
[40] H. Zhu, F. Semperlotti, Phononic thin plates with embedded acoustic black holes, Phys. Rev. B91 (10) (2015) 104304.
[41] J. Deng, O. Guasch, L. Maxit, L. Zheng, Reduction of Bloch-Floquet bending waves via annular acoustic black holes in periodically supported cylindrical shell structures, Appl. Acoust.169 (2020) 107424.
[42] X. Lyu, H. Sheng, M. He, Q. Ding, L. Tang, T. Yang, Satellite vibration isolation using periodic acoustic black hole structures with ultrawide bandgap, J. Vib. Acoust.145 (1) (2023) 014501.
[43] R. Codina, S. Badia, J. Baiges, J. Principe, Variational multiscale methods in computational fluid dynamics, Encyclopedia of Computational Mechanics (2018) 1–28.
[44] R. Codina, A stabilized finite element method for generalized stationary incompressible flows, Comput. Methods Appl. Mech. Engrg.190 (20-21) (2001) 2681–2706.
[45] R. Codina, Stabilized finite element approximation of transient incompressible flows using orthogonal subscales, Comput. Methods Appl. Mech. Engrg.191 (39-40) (2002) 4295–4321.
[46] A. Karlos, S. J. Elliott, J. Cheer, Higher-order WKB analysis of reflection from tapered elastic wedges, J. Sound Vib.449 (2019) 368–388.
[47] J. Y. Lee, W. Jeon, Exact solution of Euler-Bernoulli equation for acoustic black holes via generalized hypergeometric differential equation, J. Sound Vib.452 (2019) 191–204.
[48] D. O'boy, V. V. Krylov, Vibration of a rectangular plate with a central power-law profiled groove by the Rayleigh–Ritz method, Appl. Acoust.104 (2016) 24–32.
[49] H. Gebhardt, K. Schweizerhof, Interpolation of curved shell geometries by low order finite elements—errors and modifications, Int. J. Numer. Meth. Engrg.36 (2) (1993) 287–302.
[50] H. Hakula, Y. Leino, J. Pitkäranta, Scale resolution, locking, and high-order finite element modelling of shells, Comput. Methods Appl. Mech. Engrg.133 (3-4) (1996) 157–182.
[51] D. Choi, F. Palma, E. Sanchez-Palencia, M. Vilarino, Membrane locking in the finite element computation of very thin elastic shells, ESAIM: Math. Model. Numer. Anal. 32 (2) (1998) 131–152.
[52] A. Ambroziak, Locking effects in the finite element method, in Shell structures: Theory and application. Vol. 3, CRC Press/Balkema, 2014, p. 369.
[53] A. Aguirre, R. Codina, J. Baiges, Stress-displacement stabilized finite element analysis of thin structures using solid-shell elements—Part I: On the need of interpolating the stresses (Submitted).